Electronic Supplementary Material (ESI) for Physical Chemistry Chemical Physics.

Electronic Supplementary Information

Real-time observation of photoionization-induced water migration dynamics in 4-methylformanilide–water by picosecond time-resolved infrared spectroscopy and ab initio molecular dynamics simulations

Mitsuhiko Miyazaki, Tairiku Kamiya, Matthias Wohlgemuth, Kuntal Chatterjee, Roland Mitrić, Otto Dopfer, and Masaaki Fujii

Contents

Table S1 Substitution-induced shifts of the $S_1 \leftarrow S_0$ origin transition energies of simple mono-substituted benzenes (Bz) and toluenes (Tol).

Molecule	Δ_{00} wrt Bz (S_1 0^0)		Molecule	Δ_{00} wrt Tol (S_1 0^0)		Δ_{00}
Ph-H	– (38082)		*p*-H$_3$C-Ph-H	– (37477)		−605
Ph-F	−269 (37813)		*p*-H$_3$C-Ph-F	−617 (36860)		−953
Ph-CH$_3$	−605 (37477)		*p*-H$_3$C-Ph-CH$_3$	−744 (36733)		−744
Ph-CN	−1568 (36514)		*p*-H$_3$C-Ph-CN	−1255 (36222)		−292
Ph-OH	−1733 (36349)		*p*-H$_3$C-Ph-OH	−2140 (35337)		−1012
Ph-NHCHO	**−2078 (36004)**		***p*-H$_3$C-Ph-NHCHO**	**−2285 (35192)**		**−812**
Ph-NH$_2$	−4053 (34029)		*p*-H$_3$C-Ph-NH$_2$	−3391 (33086)		−943

Benzene: R. H. Page, et al., *J. Chem. Phys.* **88**, 5362 (1988).

Fluorobenzene: Z.- Q. Zhao and C. S. Parmenter, *J. Chem. Phys.* **96**, 6362 (1992).

Toluene: Christopher G. Hickman, et al., *J. Chem. Phys.* **104**, 4887 (1996).

Benzonitrile: R. Yamamoto, et al., *J. Raman Spectrosc.* **31**, 295 (2000).

Phenol: C. Ratzer, et al., *Chem. Phys.* **283**, 153 (2002).

Formanilide: S. Ullrich, et al., *Phys. Chem. Chem. Phys.* **4**, 2897 (2002).

Aniline: M. Honda, et al., *J. Phys. Chem.* A **107**, 3678 (2003).

p-Methylfluorobenzene: P. Butler, et al., *J. Chem. Phys.* **127**, 094303 (2007).

p-Xylene: P. J. Breen, et al., *J. Chem. Phys.* **87**, 1917 (1987).

p-Tolunitrile: M. Fujii, et al., *Spectrochim. Acta* **50A**, 1421, (1994).

p-Cresol: M. Pohl, et al., *J. Chem. Phys.* **94**, 1717 (1991).

p-Toluidine: M. Honda, et al., *J. Phys. Chem. A* **107**, 3678 (2003).

Table S2 Substitution-induced shifts of the adiabatic ionization energies of simple mono-substituted benzenes (Bz) and toluenes (Tol).

Molecule	ΔIE_0 wrt Bz (IE_0)		Molecule	ΔIE_0 wrt Tol (IE_0)		ΔIE_0
Ph-H	– (74555)		*p*-H$_3$C-Ph-H	– (71199)		−3356
Ph-CN	+3935 (78490)		*p*-H$_3$C-Ph-CN	+3946 (75145)		−345
Ph-F	−613 (73942)		*p*-H$_3$C-Ph-F	−244 (70955)		−2987
Ph-CH$_3$	−3356 (71199)		*p*-H$_3$C-Ph-CH$_3$	−2999 (68200)		−2999
Ph-OH	−5923 (68632)		*p*-H$_3$C-Ph-OH	−5281 (65918)		−2719
Ph-NHCHO	**−7147 (67408)**		***p*-H$_3$C-Ph-NHCHO**	**−6064 (65135)**		**−2237**
Ph-NH$_2$	−12274 (62281)		*p*-H$_3$C-Ph-NH$_2$	−11039 (60160)		−2121

S-1 Comparison of the 1+1′ REMPI spectrum obtained by the (ns-excitation)–(ps-ionization) scheme with the conventional nanosecond 1+1′ REMPI spectrum

Figure S1 compares REMPI spectra of (left) *trans*-AA–W and (right) *trans*-4MeFA–W obtained by different ionization schemes. The spectra recorded by the ν_{exc}(ns)+ν_{ion}(ps) scheme are essentially the same as those using the conventional ν_{exc}(ns)+ν_{ion}(ns) scheme. This result illustrates that the ν_{exc}(ns) + ν_{ion}(ps) scheme provides a much higher species selectivity comparing to that of the ν_{exc}(ps) + ν_{ion}(ps) scheme (left panel (A)), which cannot resolve vibronic bands arising from internal rotation.

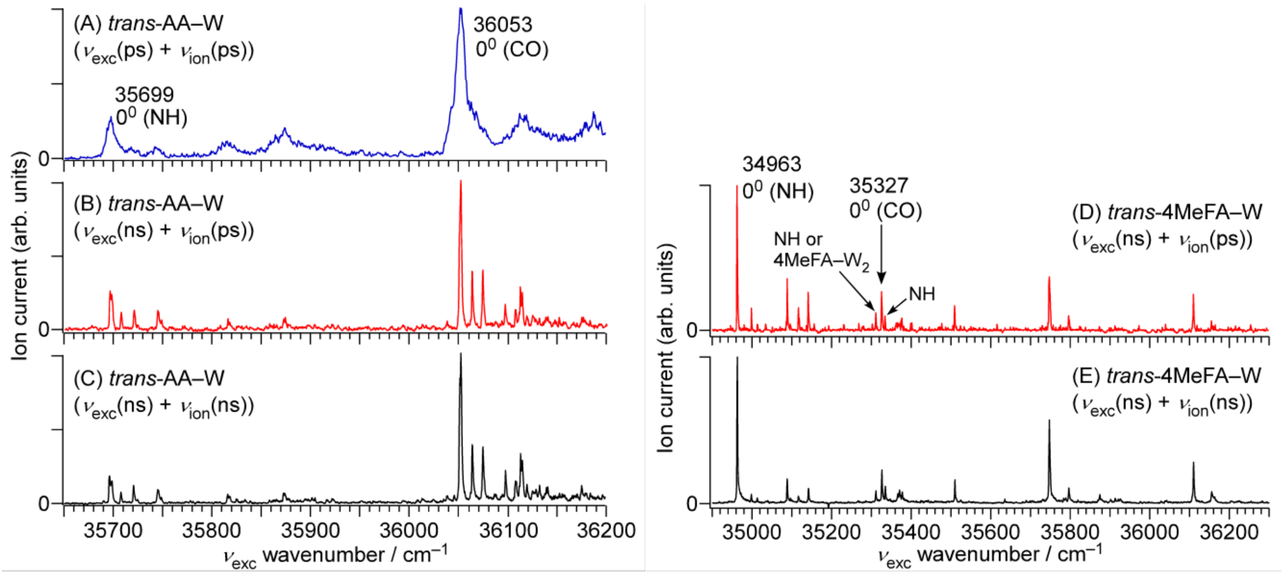

Figure S1 Comparison of REMPI spectra obtained by different excitation–ionization schemes.

(Left) REMPI spectra of *trans*-AA–W obtained by (A) (ps excitation)–(ps ionization), (B) (ns excitation)–(ps ionization), and (C) (ns excitation)–(ns ionization) schemes.

(Right) REMPI spectra of *trans*-4MeFA–W obtained by (D) (ns excitation)–(ns ionization) and (E) (ns excitation)–(ps ionization) schemes.

S-2 Lifetime of the S_1 states

Lifetime measurements were carried out by pump-probe ionization *via* the $S_1 \leftarrow S_0$ origin transition. Figure S2 shows obtained time evolutions of the ion current. Differences in the rise of the response reflect different pulse widths of the ionization lasers used for the measurements: ps laser for the tFA system, ns lasers for 4MetFA and tAA systems (different ns lasers were used for these systems), respectively.

tFA has the shortest lifetime among the measured species. The results show that both introduction of the CH_3 group and hydration elongate the lifetime, although the lifetimes almost converge at 13–14 ns. The elongation of the lifetime seems slightly larger for the CO-bound isomers than the NH-bound isomers. Changes in the interaction with the $n\pi^*$ state may have some effects on the S_1 state lifetime, because the hydrogen bonding in the CO-bound isomers partly occupies the nonbonding orbital of the C=O group.

The delay time between the (ns excitation)–(ps ionization) pulses (Δt_{UV} = 4 ns used for ps-TRIR spectroscopy) was determined to obtain the minimum pulse overlap and maximum ion signal intensity and stability.

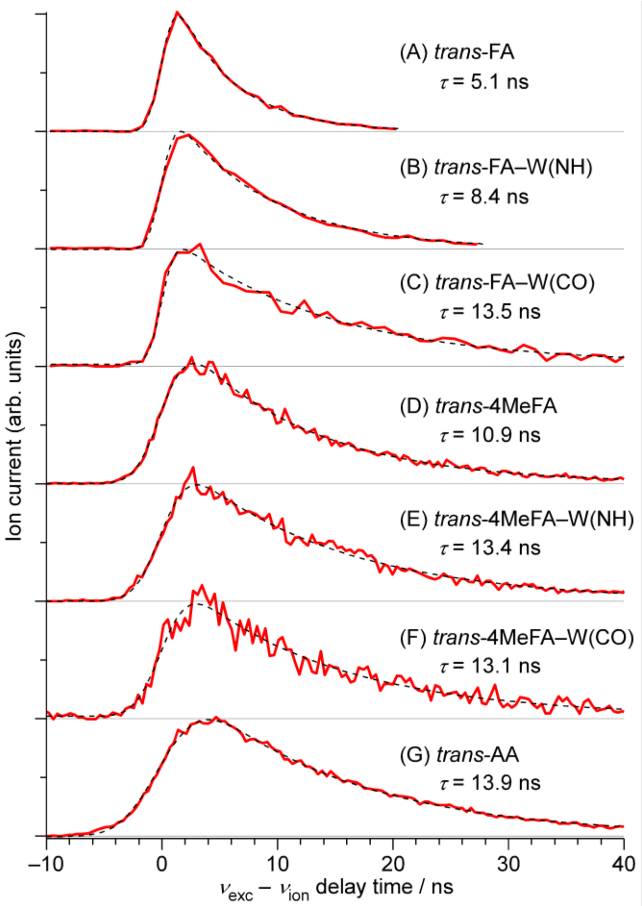

Figure S2 S_1 state population changes measured by pump-probe ionization via the $S_1 \leftarrow S_0$ origin transition. Best fits assuming a single exponential decay are shown as dashed lines. Obtained S_1 state lifetimes (τ) are noted along with the molecular and cluster isomers.

S-3 REMPI spectrum of cis-4MeFA

The $S_1 \leftarrow S_0$ origin transition of *cis*-FA is observed ~1000 cm^{-1} below that of *trans*-FA with about 50 times weaker intensity.[1] Thus, we searched the range ~1000 cm^{-1} below the origin transition of *trans*-4MeFA with a higher laser intensity. The resulting one-color REMPI spectrum is shown in Figure S3. The spectrum shows an almost equally-spaced progression similar to that of *cis*-FA, in which the long progression is ascribed to the change in the planarity of the *cis*-amide group: nonplanar in S_0, planar in S_1.[2] An expanded scan around the origin transition, however, reveals a complicated splitting that is not observed for *cis*-FA. This splitting is considered to stem from a coupling with the CH_3 internal rotation. A more detailed assignment of the structure would require higher-resolution spectroscopy.

We also tried to find hydrated *cis*-4MeFA clusters in this spectral range with a higher laser intensity. However, no signatures other than those of *trans*-4MeFA–W and overshoot depletions due to monomer transitions were detected in REMPI spectrum. Weak bands in the 34700–34900 cm^{-1} range are assigned to transitions of *trans*-4MeFA–W_2 clusters by analogy with *trans*-FA/AA–W_2 clusters. This observation is similar to that of *cis*-FA,[2] for which the hydrated cluster has been reported only from microwave spectroscopy.[3] A large hydration-induced S_1 origin shift (ca. −1000 cm^{-1} is expected for the adiabatic transition from TD-DFT calculations) and/or fast dynamics in the S_1 state (arising from coupling with a nearby nπ* state, which is also predicted by our TD-DFT calculations) may also account for this absence. Possibly, also a different ionization efficiency from these states may play an important role.

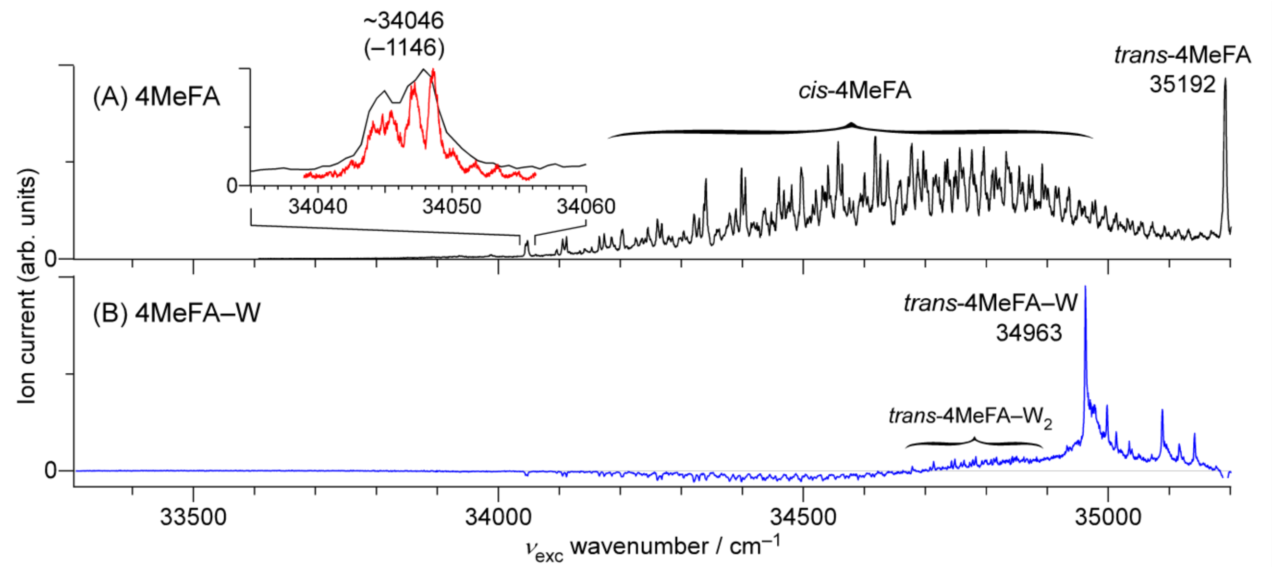

Figure S3 1+1′ REMPI spectra of (A) 4MeFA and (B) 4MeFA–W in the low-frequency range. The inset in panel (A) shows a slower and better-resolved scan of the $S_1 \leftarrow S_0$ origin band of *cis*-4MeFA. In panel (B), the same range was surveyed with a much higher laser power monitoring the 4MeFA$^+$–W cluster mass.

S-4 Photoionization efficiency (PIE) curves of 4MeFA and 4MeFA–W

Figure S4 shows PIE spectra of 4MeFA and 4MeFA–W. The PIE spectra of the monomer isomers show sharp steps at 65135 and 65521 cm^{-1} for the *trans*- and *cis*-conformers, respectively. These steps represent the adiabatic ionization energies (IE_0) of these conformers.

Similarly, the PIE spectrum of the *trans*-4MeFA–W(NH) shows some steps. The lowest energy step at 62167 cm^{-1} corresponds to IE_0. The second prominent step at IE_0 + 220 cm^{-1} is assigned to the intermolecular stretching vibration, according to the ZEKE spectrum of *trans*-FA–W(NH).[4]

The PIE spectrum of *trans*-4MeFA–W(CO), on the other hand, shows a broad rise, indicating a large structural change upon ionization. This broad feature inhibits a clear determination of IE_0, and only an upper limit is estimated as 64800 cm^{-1} from the onset of identifiable ion signal.

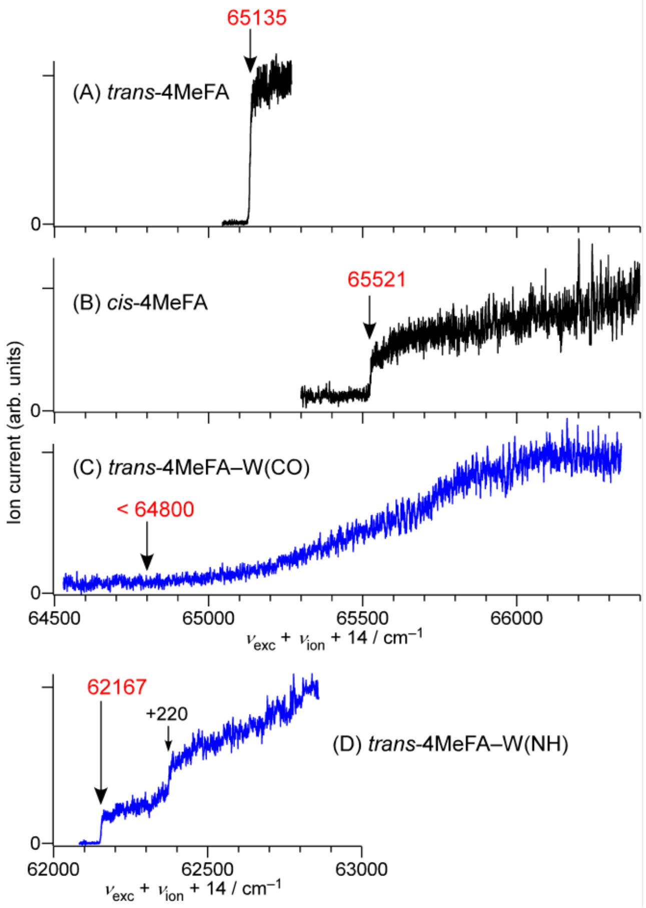

Figure S4 PIE spectra of (A) *trans*-4MeFA, (B) *cis*-4MeFA, (C) *trans*-4MeFA–W(CO), and (D) *trans*-4MeFA–W(NH). Horizontal axes of (A–C) are common, while that of (D) represents a lower frequency range. The IE_0 of each species is indicated by a vertical arrow. The horizontal axis values have been corrected for the electric field shift (14 cm^{-1}), which is determined from IE_0 of phenol measured under the same condition.[5]

S-5 Photodissociation efficiency (PDE) spectra of *trans*-4MeFA$^+$–W(CO) and *trans*-4MeFA$^+$–W(NH)

Figure S5 shows PDE curves of *trans*-4MeFA$^+$–W(CO) and *trans*-4MeFA$^+$–W(NH) obtained by monitoring the 4MeFA$^+$ fragment mass. The PDE curve of *trans*-4MeFA$^+$–W(CO) shown in Figure S4(A) gradually rises from 67140 cm^{-1}. This is considered to be (an upper bound of) the threshold of dissociation. Dissociation energies in S_0, S_1, and D_0 states are derived in combination with electronic origin shifts; these values are summarized in Figure 4 and Figure S5.

PDE measurement of *trans*-4MeFA$^+$–W(NH), on the other hand, did not provide any clear threshold value. Although the PDE spectrum in Figure S4(B-1) shows a rise starting at ~65500 cm^{-1}, the water binding energy in the S_0 state evaluated from this rise is $D_0(S_0)$ = 360 cm^{-1}, which is far too small for $H_2O\cdots H\text{-}N$ hydrogen. This rise seems to correspond to ionization of the *cis*-4MeFA monomer, because the REMPI spectrum of *cis*-4MeFA overlaps with the $S_1 \leftarrow S_0$ origin band of *trans*-4MeFA–W(NH) (see Figure S2) and the PDE spectra were monitored at the monomer mass.

PDE spectra obtained via vibronic transitions shown in panel (B-2, B-3) do not provide a clear signature for the dissociation threshold. Thus, the binding energy of *trans*-4MeFA$^+$–W(NH) could not be determined from these measurements.

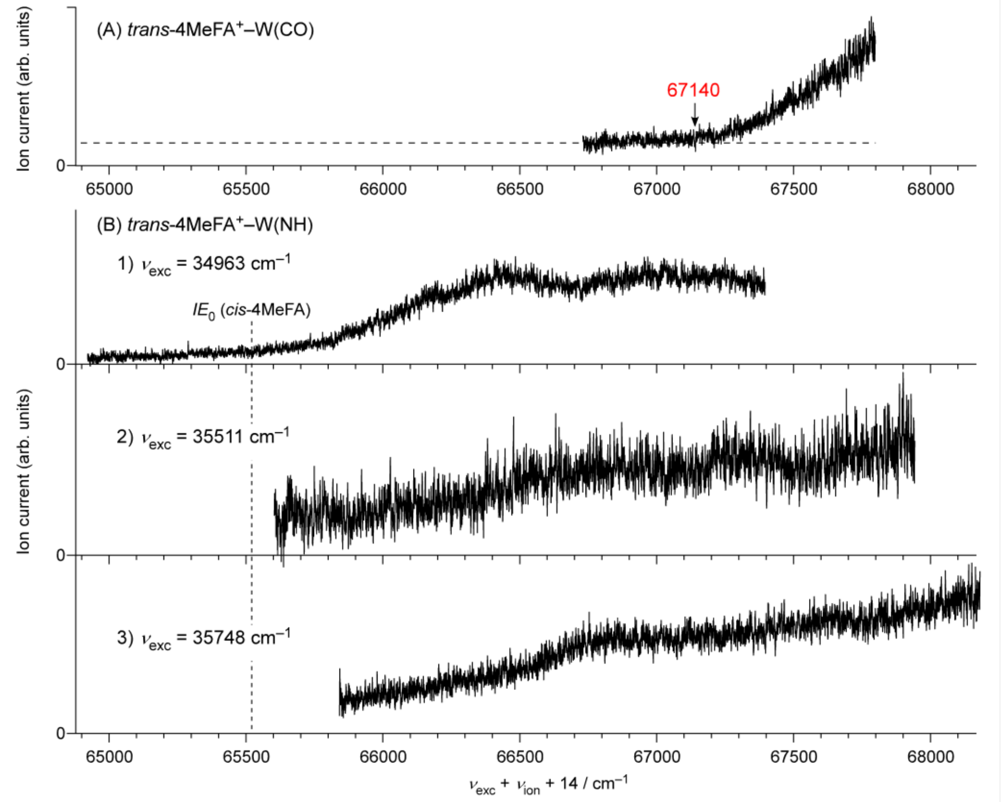

Figure S5 Photodissociation efficiency (PDE) spectra of *trans*-4MeFA$^+$–W clusters monitored at the 4MeFA$^+$ fragment mass. (A) PDE spectrum of *trans*-4MeFA$^+$–W(CO) obtained via the $S_1 \leftarrow S_0$ origin transition (35327 cm^{-1}). (B) PDE spectra of *trans*-4MeFA$^+$–W(NH) obtained via 1) the origin and 2, 3) vibronic transitions denoted in the figure. The vertical dashed line indicates IE_0 of the *cis*-4MeFA monomer (see Figure S4).

S-6 Comparison of the energy diagram of 4MeFA–W, FA–W, and AA–W

Figure S6 shows energy diagrams of 4MeFA–W (green), FA–W (blue), and AA–W (red). Values for FA–W and AA–W were collected from previous reports. Although transition energies are different for each species, the interaction energies are similar for all species, meaning similar hydrogen bonding interactions at the amide group for these molecule regardless of the modification by CH_3 substitution at either the amide or the phenyl ring.

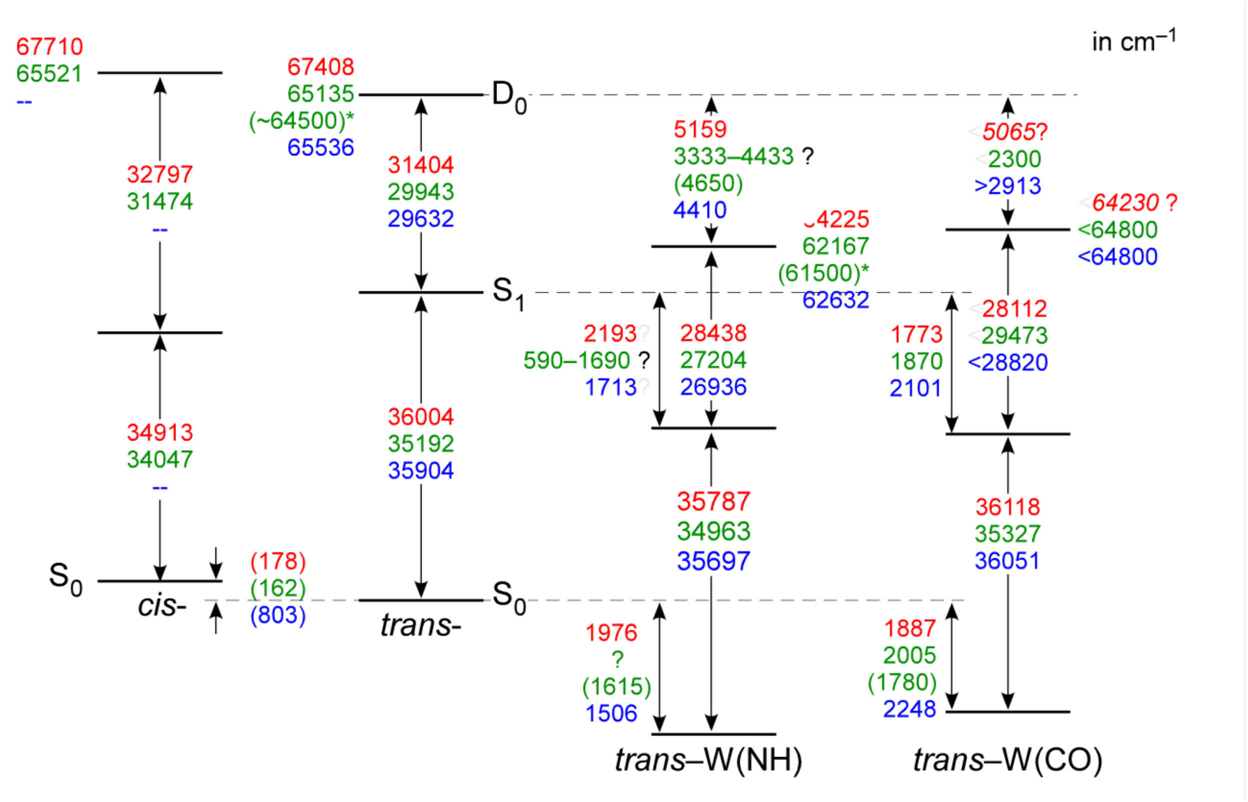

Figure S6 Energy diagrams for monohydration of AA (red), FA (blue), and 4MeFA (green) in the S_0, S_1, and D_0 states.

S-7 IR spectrum of *cis*-4MeFA

The IR spectrum of *cis*-4MeFA probed by the transition at 34049 cm^{-1} is shown in Figure S7 along with those of *trans*-4MeFA and *cis*/*trans*-FA.[6] Spectra of the same conformation coincide almost completely, and the theoretical IR spectra also reproduce well the experimental spectra, confirming that the band originates from the *cis*-conformer.

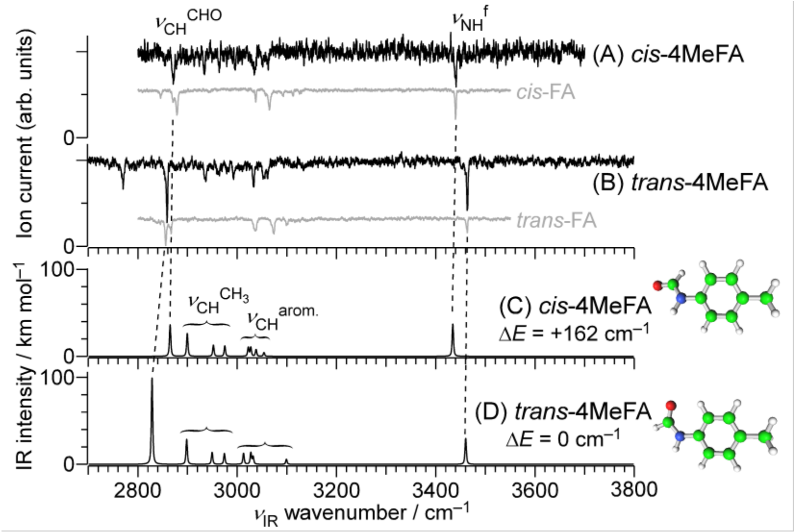

Figure S7 Experimental and computational IR spectra of (A, C) *cis*-4MeFA and (B, D) *trans*-4MeFA obtained by monitoring the origin band of each species. IR spectra of *cis*/*trans*-FA[6] are also shown for comparison. The structures and the energy difference are from calculations at CAM-B3LYP/aug-ccpVTZ with GD3BJ empirical dispersion (theoretical spectra were scaled by 0.95).

S-8 Comparison of observed and theoretical IR spectra of 4MetFA and 4MetFA–W

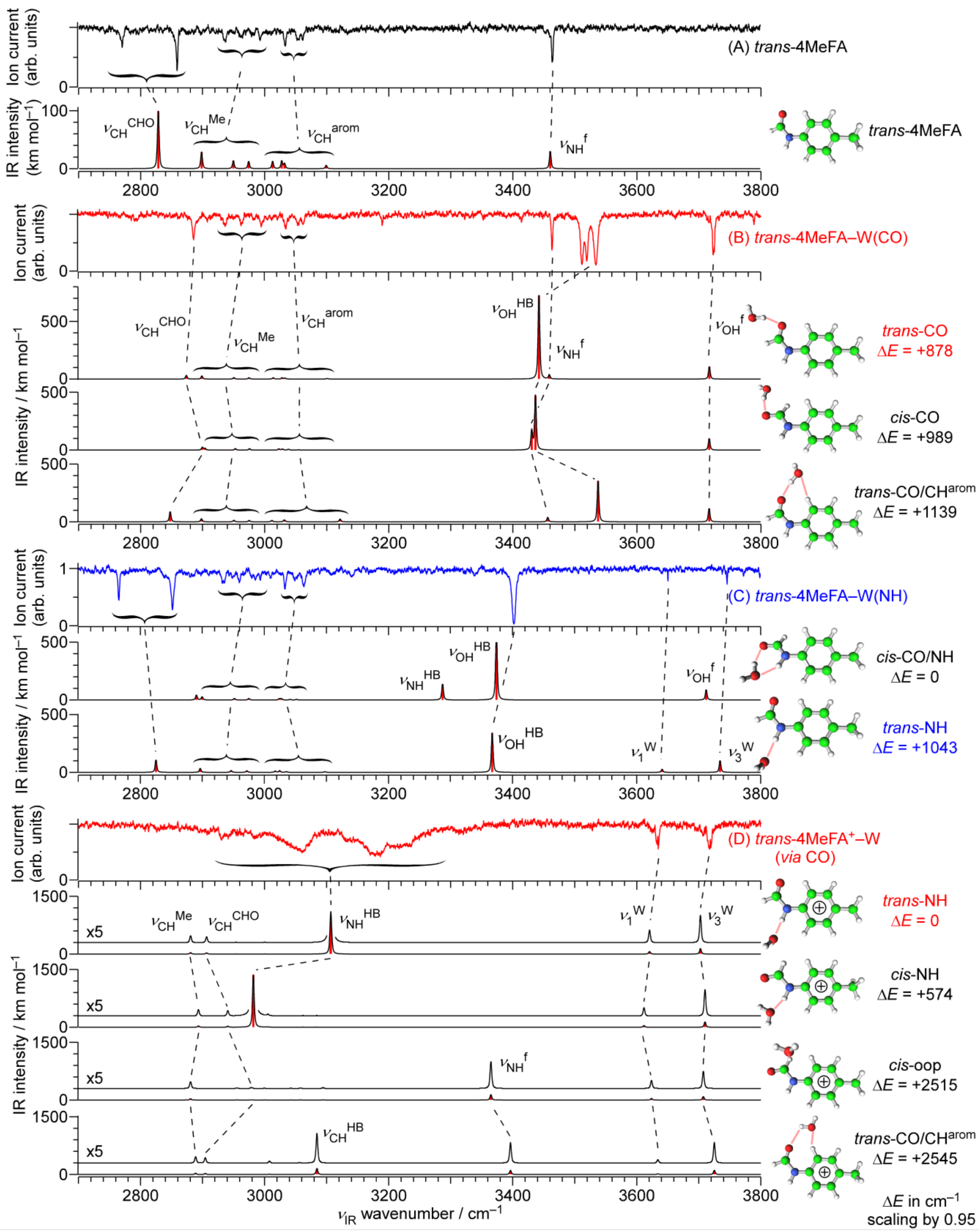

Figure S8 Comparison of observed and theoretical IR spectra of trans-4MeFA and its hydrated clusters in the S_0 and cationic D_0 states. Calculations were carried out at the level of CAM-B3LYP/ aug-cc-pVTZ with GD3BJ empirical dispersion correction. Relative energies (E_{el} + ZPE) of species (ΔE) are given in cm^{-1} together with the optimized structures. The theoretical IR frequencies were scaled by 0.95.

S-9 IR-UV hole-burning spectra of *trans*-4MeFA and *trans*-4MeFA–W

Figure S9 compares IR-UV hole-burning spectra obtained by burning IR transitions of (A) *trans*-4MeFA, (B) *trans*-4MeFA–W(CO), and (C) *trans*-4MeFA–W(NH), respectively. These IR bands are marked by an asterisk in Figure 5. All transitions in the REMPI spectrum of *trans*-4MeFA are observed in the hole-burning spectrum, confirming the single spectral carrier in this range as *trans*-4MeFA. In the monohydrated cluster, the combination of IR hole-burning spectra of the CO- and NH-bound isomers reproduces the REMPI spectrum, illustrating that these two isomers are the only species produced in the jet expansion.

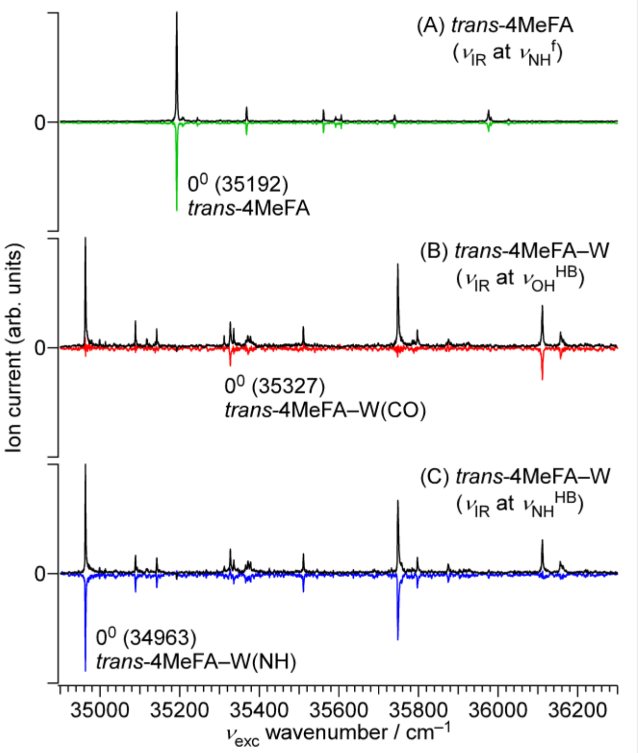

Figure S9 Comparison of REMPI and IR-UV HB spectra of (A) *trans*-4MeFA and (B, C) *trans*-4MeFA–W. IR bands used for pumping (burning) are noted in parentheses, and are marked by asterisks in Figure 5.

S-10 ps-TRIR spectra of the ionization-induced water migration in *trans*-FA–W and *trans*-AA–W

Figure S10 shows TRIR spectra of *trans*-FA–W and *trans*-AA–W recorded by the (ns excitation)–(ps ionization) scheme during the course of the photoionization-induced water migration. The spectra reproduced previous reports,[7-9] however with a better spectral quality. The bands are assigned to those of S_1 (blue), the intermediate (green), and the product (red), respectively. The assignments are confirmed by comparing to corresponding ns spectra shown in the top (S_1) and bottom (product) panels.

The S_1 transition of *trans*-AA–W was originally interpreted as ν_{OH}^{HB} of the Franck-Condon (FC) state populated in the cationic state.[9] However, the assignment should be revised to that in the S_1 state according to the result of the present measurement. The wrong assignment was caused by the limited ability in state specification of the (one-color) (ps excitation)–(ps ionization) scheme used in the previous work,[9] in which the

FC state and intermediate S$_1$ state are not separable. The new (ns excitation)–(ps ionization) scheme used herein clearly assigns the origin of this spectral feature to the S$_1$ state. This result illustrates the superiority of this method (ns-ps versus ps-ps), in addition to the higher species selectivity owing to the ns excitation step.

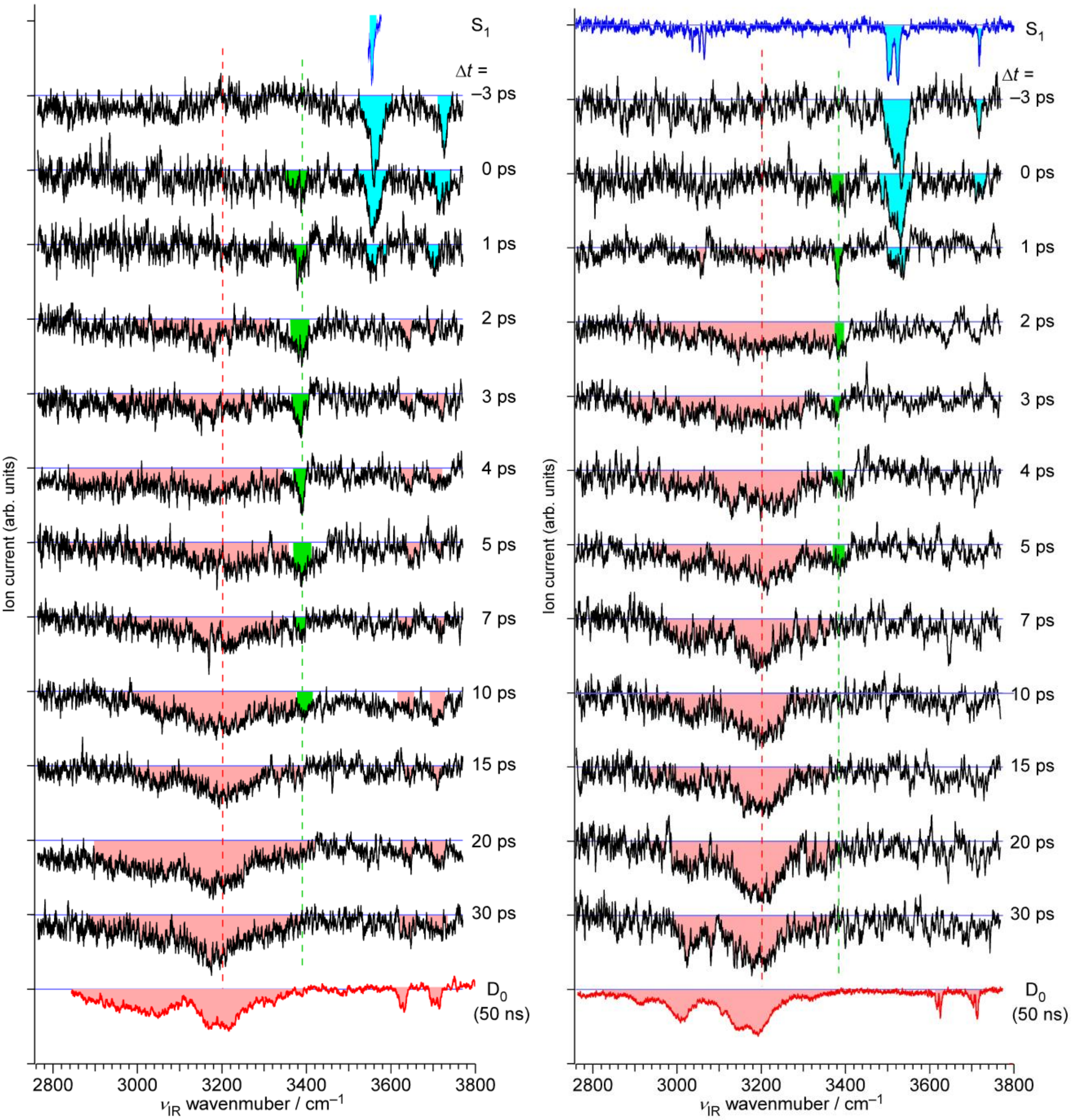

Figure S10 The ps-time resolved IR (ps-TRIR) spectra of (left) *trans*-FA$^+$–W and (right) *trans*-AA$^+$–W recorded by the (ns excitation)–(ps ionization) scheme. The top and bottom traces show stationary (ns) IR spectra in the S$_1$ and D$_0$ states, respectively. The IR spectrum of *trans*-FA–W in the S$_1$ state is taken from ref. [10], and that in the D$_0$ state is taken from ref. [7].

S-11 Comparison of the time evolutions of the ν_{NH}^{f} and ν_{NH}^{HB} bands in the ionization-induced water migration of *trans*-4MeFA$^+$–W, *trans*-FA$^+$–W, and *trans*-AA$^+$–W

Figure S9 shows time evolutions (TEs) of the ps-TRIR spectra monitored at ν_{NH}^{f} and ν_{NH}^{HB}, respectively. These traces almost reproduce those of the previous reports. The best fits simulated by using kinetic models match the experimental traces well. Time constants obtained from the fits are summarized in Table 3. The uncertainty (ca. ±2 ps) stems from the experimental limitations on the reproducibility (e.g. signal fluctuation, alignment of laser beams) and not from the fitting process.

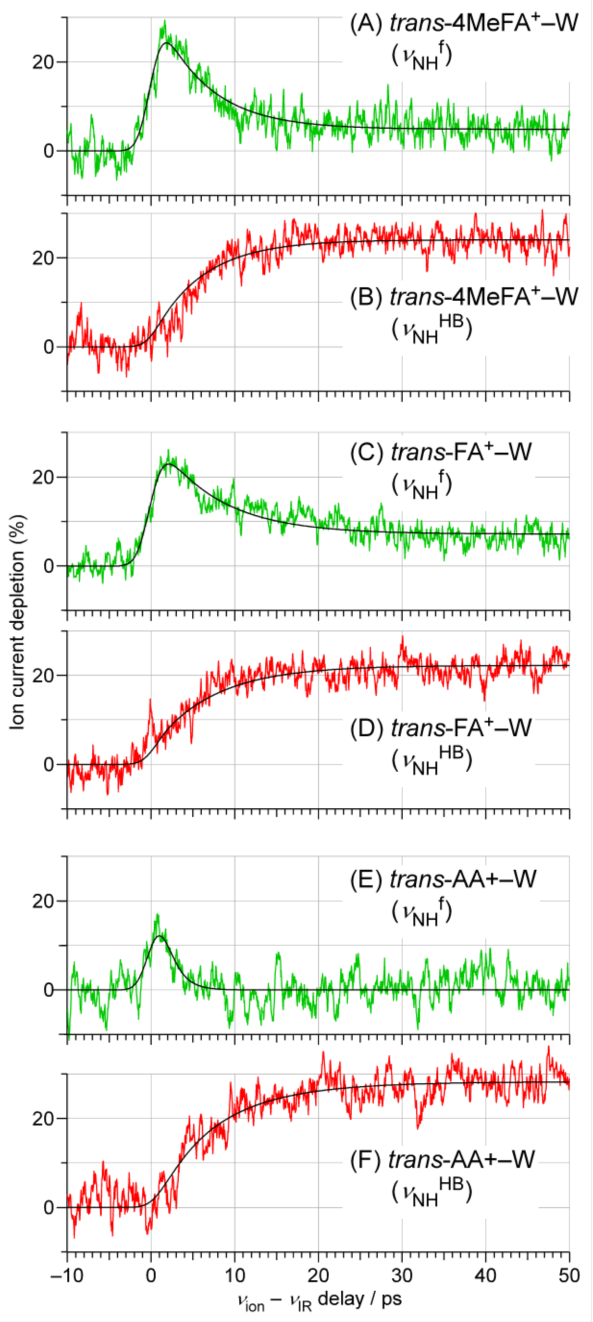

Figure S11 Time evolutions of the ν_{NH}^{f} and ν_{NH}^{HB} vibrations for the ionization-induced water migration of (A, B) *trans*-4MeFA$^+$–W (reproduction of Figure 7), (C, D) *trans*-FA$^+$–W, and (E, F) *trans*-AA$^+$–W clusters obtained by the (ns excitation)–(ps ionization) scheme. The probed frequencies are shown in Figure S10. Best fits are also shown (in black). Details of the fitting are described in S-13.

S-12 Theoretical calculations of the methyl group internal rotation potentials and their rotational energy levels for *trans*-4MeFA$^+$ and *trans*-AA$^+$.

Figure S12 shows the CH_3 internal rotation potentials and their rotational energy levels for (A, C) 4MetFA$^+$ and (B, D) tAA$^+$ obtained at the CAM-B3LYP/aug-cc-pVTZ level of theory and by diagonalization of the potential using the free rotation eigen functions. The height of the rotational potential barrier of 4MetFA$^+$ is ~7 cm^{-1}, and thus the CH_3 group is regarded as a nearly free rotator. On the other hand, the rotational barrier of tAA$^+$ is rather high (~240 cm^{-1}), and thus the CH_3 group cannot rotate freely at low-temperature conditions. Simulated energy levels reproduce the experimental values reasonably well, and some low energy states are summarized in Table S3.

Excess energies deposited by the photoionization of the CO-bound monohydrated clusters are expected to become ca 5000 cm^{-1}. In such a high energy state, the rotational motion does not feel a minor change in the potential any more, and can be treated as free rotation for both the species. For example, rotational energies of a free rotator with $B = 5.2$ cm^{-1} at $m = 20$ and $m = 30$ are $E_{\mathrm{rot}} = B\, m^2 = 2080$ cm^{-1} and 4680 cm^{-1}. These values are well match with energy levels of 4MetFA$^+$ and tAA$^+$ as shown in Figure S10 (C, D). This result justifies our vDOS estimation that regards the -CH_3 group as an independent free rotor.

Table S3 Methyl internal rotation states of *trans*-4MeFA$^+$ and *trans*-AA$^+$ estimated from potential calculations at the CAM-B3LYP/aug-cc-pVTZ level of theory compared to experimental values.

state	*trans*-4MeFA$^+$	*trans*-AA$^+$	*trans*-AA$^+$ (*trans*-AA$^+$–W)[a]
	Calculation[a] / cm^{-1}	Calculation[a] / cm^{-1}	Experiment / cm^{-1}
0a	0 (3)	0 (51)	0 (0)
1e	5 (8)	0 (51)	0 (0)
2e	21 (24)	93 (144)	110 (103)
3a$_1$	48 (51)	157 (208)	200 (175)
4e	83 (86)	171 (222)	208 (208)
5e	130 (133)	216 (268)	261 (265)
20e	2080 (2083)	2151 (2202)	
30a	4680 (4683)	4750 (4801)	

[a] Absolute energies in parentheses. ref. [11, 12]

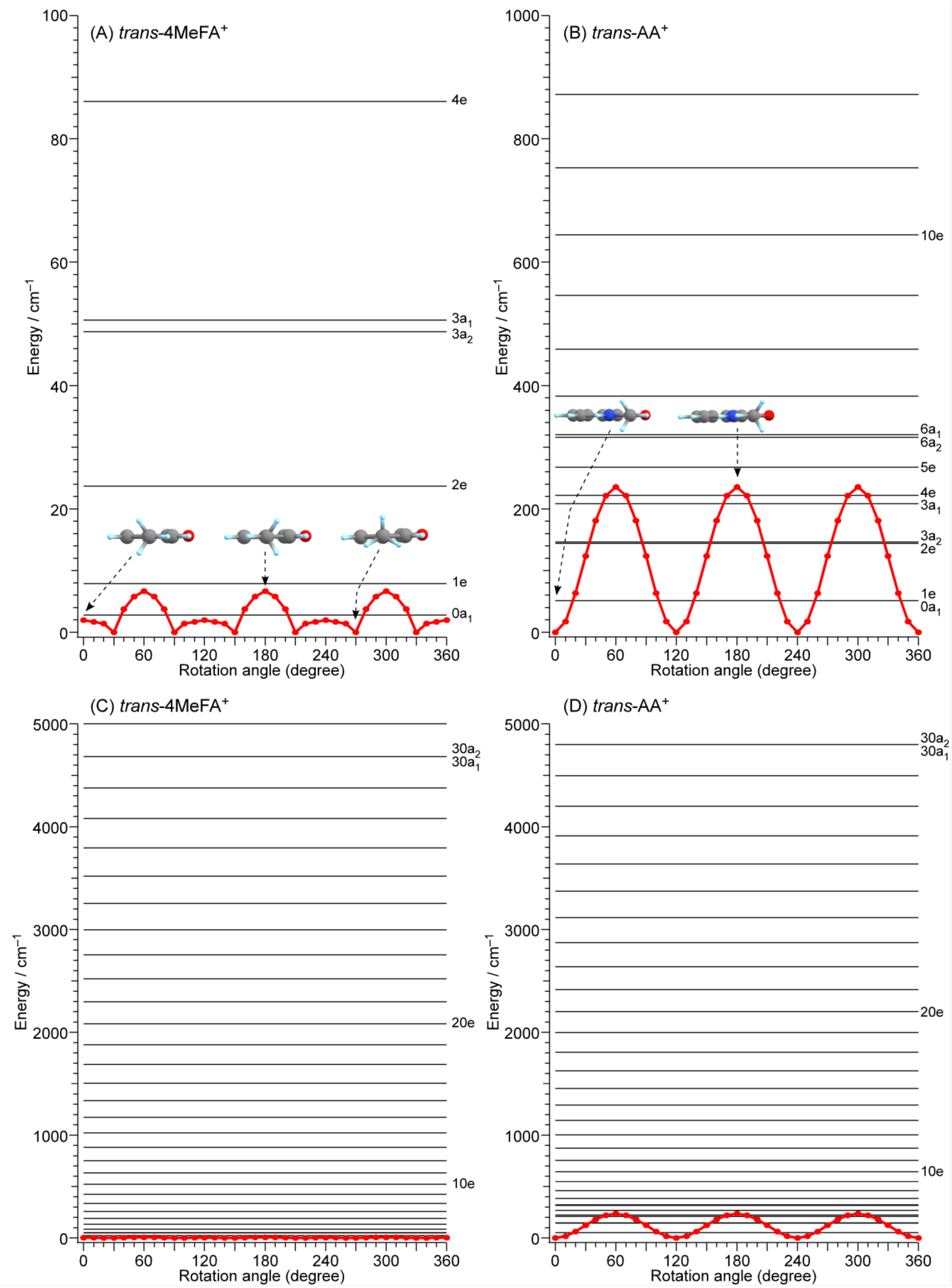

Figure S12 Internal rotation potentials of the CH_3 group and their rotational energy levels for (A, C) *trans*-4MetFA$^+$ and (B, D) *trans*-AA$^+$ (CAM-B3LYP/aug-cc-pVTZ level).

S-13 Solutions of the rate equations for the proposed reaction schemes

Here, we define the concentration of the species involved in the water migration reaction as follows:

$[\mathrm{R}^+]$ ≡ CO-bound structure (FC state of photoionization)

$[\mathrm{P}^+ (\mathrm{hot})]$ ≡ NH-bound product structure (with high translational energy)

$[\mathrm{I}^+]$ ≡ Intermediate (structures without hydrogen bonding)

$[\mathrm{P}^+ (\mathrm{cold})]$ ≡ NH-bound product structure (with low translational energy)

Rate equations for the model shown in Figure 8 in the main text are

$$\frac{\mathrm{d}[\mathrm{R}^+]}{\mathrm{d}t} = -k_1[\mathrm{R}^+] \qquad \text{(S1)},$$

$$\frac{\mathrm{d}[\mathrm{P}^+(\mathrm{hot})]}{\mathrm{d}t} = k_1[\mathrm{R}^+] - (k_2 + k_4)[\mathrm{P}^+(\mathrm{hot})] + k_3[\mathrm{I}^+] \qquad \text{(S2)},$$

$$\frac{\mathrm{d}[\mathrm{I}^+]}{\mathrm{d}t} = k_2[\mathrm{P}^+(\mathrm{hot})] - k_3[\mathrm{I}^+] \qquad \text{(S3)},$$

$$\frac{\mathrm{d}[\mathrm{P}^+(\mathrm{cold})]}{\mathrm{d}t} = k_4[\mathrm{P}^+(\mathrm{hot})] \qquad \text{(S4)},$$

where $k_i = {\tau_i}^{-1}$.

Solutions of the equations for the initial conditions of $[\mathrm{R}^+](t = 0) = [\mathrm{R}^+]_0$ and $[\mathrm{P}^+ (\mathrm{hot})](t = 0) = [\mathrm{I}^+](t = 0) = [\mathrm{P}^+ (\mathrm{cold})](t = 0) = 0$ are as follows:

$$\frac{[R^+]}{[R^+]_0} = e^{-k_1 t} \qquad \text{(S5)},$$

$$\frac{[P^+(\mathrm{hot})]}{[R^+]_0} = k_1\left[-\frac{(k_1 - k_3)e^{-k_1 t}}{(k_1 - \alpha)(k_1 - \beta)} - \frac{(k_3 - \alpha)e^{-\alpha t}}{(k_1 - \alpha)(\alpha - \beta)} + \frac{(k_3 - \beta)e^{-\beta t}}{(k_1 - \beta)(\alpha - \beta)}\right] \qquad \text{(S6)},$$

$$\frac{[I^+]}{[R^+]_0} = k_1 k_2\left[\frac{e^{-k_1 t}}{(k_1 - \alpha)(k_1 - \beta)} - \frac{e^{-\alpha t}}{(k_1 - \alpha)(\alpha - \beta)} + \frac{e^{-\beta t}}{(k_1 - \beta)(\alpha - \beta)}\right] \qquad \text{(S7)},$$

$$\frac{[P^+(\mathrm{cold})]}{[R^+]_0} = k_1 k_4\left[-\frac{(k_1 - k_3)(1 - e^{-k_1 t})}{k_1(k_1 - \alpha)(k_1 - \beta)} - \frac{(k_3 - \alpha)(1 - e^{-\alpha t})}{(k_1 - \alpha)(\alpha - \beta)\alpha} + \frac{(k_3 - \beta)(1 - e^{-\beta t})}{(k_1 - \beta)(\alpha - \beta)\beta}\right] \qquad \text{(S8)},$$

where

$$\alpha = \frac{k_2 + k_3 + k_4 + \sqrt{(k_2 + k_3 + k_4)^2 - 4k_3 k_4}}{2},$$

$$\beta = \frac{k_2 + k_3 + k_4 - \sqrt{(k_2 + k_3 + k_4)^2 - 4k_3 k_4}}{2}.$$

Equations (S5–S8) were convoluted by a Gaussian function that represents the instrumental function. Because $[\mathrm{R}^+]$ and $[\mathrm{I}^+]$ contribute to $\nu_{\mathrm{NH}}{}^{\mathrm{f}}$ with some overlap of the tails of $\nu_{\mathrm{NH}}{}^{\mathrm{HB}}$ from $[\mathrm{P}^+(\mathrm{hot})]$ and $[\mathrm{P}^+(\mathrm{cold})]$, and $[\mathrm{P}^+(\mathrm{hot})]$ and $[\mathrm{P}^+(\mathrm{cold})]$ contribute to $\nu_{\mathrm{NH}}{}^{\mathrm{HB}}$ (but with somewhat different absorption intensities), linear combinations were made for the fitting. The coefficients of the liner combinations in addition to the rate constants were optimized during the fitting.

S-14 Schematic diagram of the tier model [13]

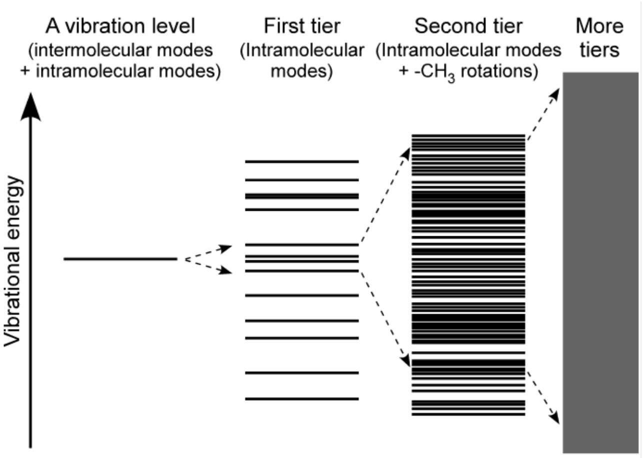

Figure S13 Schematic diagram of the tier model for the IVR of via the CH_3 internal rotation.[13] A vibrational level that is highly excited in the intermolecular modes interacts with the first tier, which is constructed mainly by intramolecular modes of $4MeFA^+$. The first tier interacts with the second tier, the density of which is high due to existence of the low-frequency CH_3 internal rotational levels. The high vibrational density of states in the second tier accelerates the IVR rate.

References

1 V. P. Manea, K. J. Wilson and J. R. Cable, *J. Am. Chem. Soc.*, 1997, **119**, 2033-2039.

2 J. A. Dickinson, M. R. Hockridge, E. G. Robertson and J. P. Simons, *J. Phys. Chem. A*, 1999, **103**, 6938-6949.

3 P. Pinacho, S. Blanco and J. C. López, *Phys. Chem. Chem. Phys.*, 2019, **21**, 2177-2185.

4 S. Ullrich, X. Tong, G. Tarczay, C. E. H. Dessent and K. Müller-Dethlefs, *Phys. Chem. Chem. Phys.*, 2002, **4**, 2897-2903.

5 S. Ullrich, G. Tarczay and K. Müller-Dethlefs, *J. Phys. Chem. A*, 2002, **106**, 1496-1503.

6 M. Miyazaki, J. Saikawa, H. Ishizuki, T. Taira and M. Fujii, *Phys. Chem. Chem. Phys.*, 2009, **11**, 6098-6106.

7 M. Wohlgemuth, M. Miyazaki, K. Tsukada, M. Weiler, O. Dopfer, M. Fujii and R. Mitrić, *Phys. Chem. Chem. Phys.*, 2017, **19**, 22564-22572.

8 M. Wohlgemuth, M. Miyazaki, M. Weiler, M. Sakai, O. Dopfer, M. Fujii and R. Mitrić, *Angew. Chem. Int. Ed.*, 2014, **53**, 14601-14604.

9 K. Tanabe, M. Miyazaki, M. Schmies, A. Patzer, M. Schütz, H. Sekiya, M. Sakai, O. Dopfer and M. Fujii, *Angew. Chem. Int. Ed.*, 2012, **51**, 6604-6607.

10 E. G. Robertson, *Chem. Phys. Lett.*, 2000, **325**, 299-307.

11 S. Ullrich and K. Müller-Dethlefs, *J. Phys. Chem. A*, 2002, **106**, 9181-9187.

12 S. Ullrich and K. Müller-Dethlefs, *J. Phys. Chem. A*, 2002, **106**, 9188-9195.

13 R. H. Page, Y. R. Shen and Y. T. Lee, *J. Chem. Phys.*, 1988, **88**, 4621-4636.